Journal of
Materials Chemistry A

Accepted Manuscript

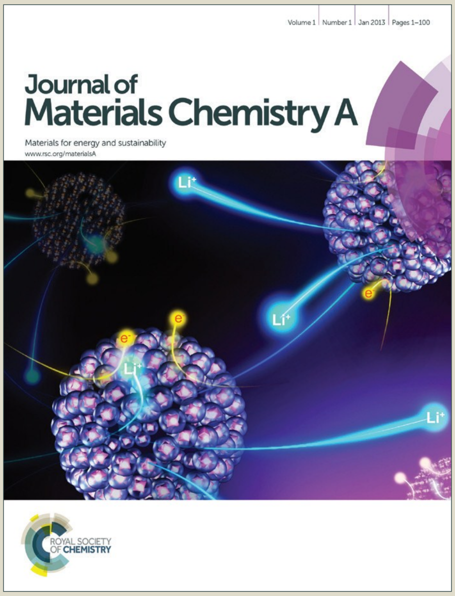

Volume 1 | Number 1 | Jan 2013 | Pages 1–100

Journal of
Materials Chemistry A

Materials for energy and sustainability
www.rsc.org/materialsA

ROYAL SOCIETY
OF CHEMISTRY

ROYAL SOCIETY
OF CHEMISTRY

www.rsc.org/materialsA

Journal Name

ARTICLE

Binder-free graphene as advanced anode for lithium batteries

Haiyan Sun[a], Antonio Esau Del Rio Castillo[a], Simone Monaco[b], Andrea Capasso[a], Alberto Ansaldo[a], Mirko Prato[b], Duc Anh Dinh[a]; Vittorio Pellegrini[a], Bruno Scrosati[b], Liberato Manna[b] and Francesco Bonaccorso[a]*

Received 00th January 20xx,
Accepted 00th January 20xx

DOI: 10.1039/x0xx00000x

www.rsc.org/

We report the fabrication of binder-free anodes for lithium-ion batteries (LIBs) based on graphene nanoflakes on-demand designed and produced by liquid phase exfoliation of graphite. A solvent exchange process is exploited to first remove the N-Methyl-2-Pyrrolidone used for the exfoliation of graphite and then to re-disperse the exfoliated single- (SLG) and few-layer (FLG) graphene flakes, at a high concentration (~5 g L^{-1}), in an environmentally-friendly solvent, *i.e.,* ethanol. Anodes are realized by drop-casting the SLG- and FLG-based ink in ethanol at ambient conditions on a copper foil without any binder or conductive agents, typically used for the fabrication of conventional LIBs. We test our SLG- and FLG-based anodes in a half-cell configuration, achieving a reversible specific capacity of ~500 mAh g^{-1} after 100 cycles at a current density of 0.1 A g^{-1}, with coulombic efficiency >99.5 %. We also test the SLG- and FLG-based anode in a full-cell configuration, exploiting commercial LiNi$_{0.5}$Mn$_{1.5}$O$_4$ as cathode. The battery operates around 4.7 V with a flat-plateau voltage profile and a reversible specific capacity of ~100 mAh g^{-1}. The proposed electrode fabrication process is fast, low cost and industrially scalable opening the way to the optimization of energy and power densites, lifetime and safety of LIBs, while minimizing their cost and environmental impact.

Introduction

In the last decades, lithium-ion batteries (LIBs) have become one of the most popular energy storage technologies, especially in consumer electronics, an increasingly growing market driven by the widespread diffusion of portable electronic devices.[1-3] The demand of LIBs will grow even more with the rise of electric vehicles (hybrid or full-electric), in view of a shift from fuel-burning to more sustainable energy sources for transportation[4] and in accordance with the worldwide agreement on the CO$_2$ emissions reduction.[5] A LIB, in its most conventional structure, consists of a graphite anode, a cathode (formed by a lithium metal oxide), and an electrolyte embedded in a separator.[6] During the charging process, lithium ions are de-intercalated from the cathode to the electrolyte and, passing through the separator, are then intercalated into the anode; during the discharge phase, this process is reversed.[7-9] Although the electrochemical performances of LIBs are influenced by the properties/quality of all the constituents, e.g., electrolyte, separator and current-collector, the electrodes play a key role.[10]

One of the critical challenges that LIBs technology is currently facing is the development of high-performance anodes,[2] capable to yield high specific capacity and energy efficiency, coupled with long cycle life and low cost, in order to meet the environmental constraints and ultimately to suit the needs of industrial-scale production.[6, 11] Conventional LIB anodes are commonly composed by ~60-90 % of active material,[12] a conductive material to increase the electrical conductivity of the electrodes, and a binder exploited to enhance the adhesion between the active material and the current-collector support.[13]

The main limiting factor of the most conventional active anode material, graphite,[4] relies in its theoretical maximum specific capacity of 372 mAh g^{-1}.[14] In this context, there is a significant interest in replacing graphite with a higher specific capacity anode material, such as other carbon derivatives[15] (*i.e*, carbon nanotubes -CNT-[16] and reduced graphene oxide -RGO-[17, 18]), alloying-type materials (e.g., Sn[19], Si[20, 21], Ge[22]), and transition metal oxides (e.g., FeO[10], CoO[10], NiO[10], Cu$_2$O[10], MnO[9, 23] and Co$_3$O$_4$[24-26]). However, most of the aforementioned materials[9, 10, 20-25] are currently unsuitable to be scaled up to the industrial level due to various issues. RGO, for example, presents poor electrochemical stability and a high irreversible specific capacity due to the large amount of structural defects and functional groups;[27] Si and Sn alloys suffer a high specific capacity fade due to their large volume expansion/contraction during charge-discharge cycling;[28] while nanocrystalline transition metal oxides usually require time-consuming synthesis processes.[23, 29]

---

[a] *Graphene Labs, Istituto Italiano di Tecnologia, via Morego 30, 16163 Genova, Italy*

[b] *Nanochemistry, Istituto Italiano di Tecnologia, via Morego 30, 16163 Genova, Italy*

† *email:francesco.bonaccorso@iit.it*

See DOI: 10.1039/x0xx00000x

Graphene nanoflakes prepared by liquid phase exfoliation (LPE) of graphite are emerging as a promising anode material for LIB,[30] having both high specific surface area[31] and electrical conductivity,[30, 32-34] which translate into a high specific capacity of ~750 mAh g^{-1} at a current density of 700 mA g^{-1} thanks to the uptake of Li ions both on the basal planes and on the edges.[30] However, the most-effective solvents for the production of graphene nanoflake-based inks,[35] such as N-Methyl-2-Pyrrolidone (NMP),[11, 36, 37] N,N-Dimethylformamide,[38] N,N-Dimethylacetamide,[39] just to cite a few, are not environmentally friendly.[37, 40] These issues are posing a severe limitation for the exploitation of graphene nanoflake-based inks in LIB technology as well as in other devices for energy conversion and storage.[1] Moreover, all the aforementioned solvents have high boiling point (>150 °C),[41] and their evaporation usually requires high temperature (e.g., 400 °C)[23] coupled with high vacuum conditions to avoid the oxidation of the graphene nanoflakes.[35, 37] Non-toxic and low-boiling point solvents such as water[42-44] and some alcohols,[45] which would be crucial to develop a fully environmentally-compatible deposition/coating processes,[35, 37] require the addition of stabilizing agents, i.e., polymers or surfactants,[44, 46] for the optimal dispersion of the flakes. Unfortunately, the presence of such stabilizers in the ink compromises the graphene nanoflakes electrochemical properties once deposited onto the current collector.[34] A viable strategy to overcome the aforementioned issues relies in the exploitation of co-solvents (e.g., water/ethanol,[37, 47, 48] and water/isopropanol[48-50]) to tune the rheological properties of low-boiling point solvents for the formulation of graphene nanoflake-based inks. However, the concentration of the as-produced ink is still low (<1 g L^{-1}),[37, 49, 50] thus not ideal for applications where highly concentrated ink is needed, *i.e.*, the production of battery electrodes.

Besides the issues on the development of novel and high-performant anode materials, advances in the electrode fabrication processes[51-58] are also needed. In fact, the electrode preparation[13, 59] is time consuming and expensive, with a strong impact on the cost of the LIBs technology.[60-62] Additionally, the composition and morphology of the electrode are critical for the battery operation, because both composition and morphological inhomogeneity can hinder the diffusion of Li ions throughout the electrode itself, determining a high charge transfer resistance value of the battery.[63] Finally, the weight of the binder, being a material not involved in the lithiation/de-lithiation processes,[64] has a negative effect on the electrochemical performance of the anode, limiting both the specific capacity and the energy density of the battery.[64] In this context, for example, polyvinylidene fluoride (PVdF), *i.e.*, the widely used binder material,[6] is reported to swell (e.g., PVdF binder in Si battery has shown a 20% thickness change in electrolyte during the charge/discharge process)[65] in contact with electrolytes based on carbonate solvents.[65] This effect determines the solvent decomposition with consequent capacity fading of the battery during operation.[65-68] In this regard, it is necessary to envisage novel production processes for the anodes.[60]

There is a fervent research activity[51-58] in the development of binder-free anode electrodes, mostly exploiting the direct deposition of the active materials on the current collector.[51-55] However, most of the proposed methods, such as electrophoretic deposition of hollow Co_3O_4[51], sputtering of Ge embedded in a carbon matrix[52] and chemical vapour deposition (CVD) of CNT[53] and Si nanowires,[54] as well as microwave plasma enhanced CVD of vertically aligned graphene sheet,[55] are not meeting yet the market requirements in term of scalability and low-cost production.[60] Another route, *i.e.*, vacuum filtration,[56, 57] has been reported for the preparation of carbon-based binder-free anodes, so called free-standing electrodes,[56-58] without any current collector support substrate. However, these anodes present various limitations, i.e., a large irreversible capacity (~1000 mAh g^{-1} for single-wall CNT[57]), as well as low reversible capacity (*e.g.*, ~300 mAh g^{-1} for RGO paper[56] and ~330 mAh g^{-1} for hybrid CNT/RGO[58]).

Here, we report on the successful one-step fabrication of LIB anodes by drop-casting on a Cu foil at room temperature (RT) an environmentally-friendly graphene nanoflake-based ink without the addition of conductive additives, *e.g.*, carbon black and binders, thus avoiding the conventional time-consuming preparation and deposition of the anode electrodes.[12, 13, 59] The graphene ink is prepared by LPE of pristine graphite in NMP, to guarantee a high quality (in term of lateral size and thickness) of the exfoliated flakes.[30] A solvent exchange process[69] is then used to first remove the NMP and then re-disperse the exfoliated flakes, at a high concentration (~5 g L^{-1}), in an environmentally-friendly solvent, *i.e.*, ethanol. The graphene nanoflake-based anodes are tested in half-cell configuration, achieving a reversible specific capacity of 503 mAh g^{-1} after 100 cycles. Moreover, we demonstrate that our fast, low cost and industrially scalable graphene nanoflakes electrode fabrication has potentiality also in a LIB configuration. Exploiting commercial $LiNi_{0.5}Mn_{1.5}O_4$ (LNMO) as cathode material and our graphene nanoflake-based anode, we have achieved a reversible specific capacity of the battery of ~100 mAh g^{-1}, opening the way to the optimization of energy/power densities and lifetime environmentally friendly LIBs.

Experimental

Inks preparation

Liquid phase exfoliation of graphite in NMP. 1 g of graphite flakes (Sigma-Aldrich) is dispersed in 100 mL of NMP (Sigma-Aldrich) and exfoliated by ultrasonication in a sonic bath (Branson®5800) for 6 hours (see Fig. 1(a)). The resulting dispersion is then ultracentrifuged at 10000 rpm (in a Beckman Coulter Optima™ XE-90 with a SW32Ti rotor) for 30 min. at 15 °C, to remove thick flakes and un-exfoliated graphite (see Fig. 1(b)).[30, 36, 44] After the ultracentrifugation process, the supernatant is collected by pipetting, thus delivering a graphene dispersion in NMP.

Solvent-exchange process. 100 mL of graphene dispersed in NMP are filtrated through a Millipore® filter with 0.2 µm pore size by vacuum filtration (see Fig. 1 (c)). Meanwhile 1 L of ethanol (Sigma-Aldrich, ≥99.8 %) is added in batches of 100 mL each to the filtration flask. Finally, 5 mL of ethanol are used to recover the graphitic flakes from the filter and 10 min of sonication is then applied to re-disperse the graphitic flakes in ethanol. The NMP solvent is then

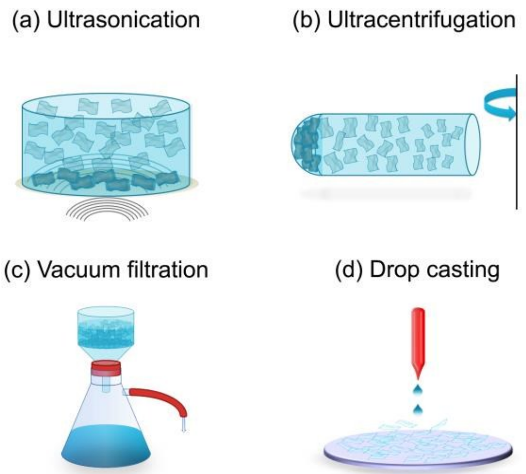

Figure 1. Schematic representation of the graphene ink production and electrode fabrication. (a) Liquid phase exfoliation of graphite by the ultrasonication process in NMP. (b) Size selection of graphene flakes carried out by ultracentrifugation. (c) Solvent exchange process. The graphene ink in NMP is exchanged in ethanol via vacuum filtration. (d) Drop-casting of the graphene ink in ethanol onto the Cu substrate.

recycled after the filtration process and re-used for another exfoliation process of graphite.

Inks characterization

Optical absorption spectroscopy (OAS) is carried out by a Cary Varian 5000UV-Vis. The graphitic ink in NMP is diluted to 1:20 with pure NMP. Afterwards, the diluted ink is placed inside the quartz cuvette used for the OAS. The concentration of the ink is determined considering the experimentally derived absorption coefficient of 1390 L $g^{-1}m^{-1}$ at 660 nm.[11, 36]

Transmission electron microscopy (TEM) images are taken with a JOEL JEM 1011 transmission electron microscope, operated at 100 kV. The graphitic ink in NMP is then diluted 1:10 with pure NMP, while the one in ethanol is diluted 1:200 with pure ethanol. 100 µL of the resulting inks are drop-cast at RT onto carbon coated copper TEM grids (300 mesh), rinsed with deionized (DI) water and subsequently dried under vacuum overnight.

Raman measurements are carried out with a Renishaw 1000 using a 50X objective, a laser with a wavelength of 532 nm and an incident power of~1 mW. The D, G and 2D peaks are fitted with Lorentzian functions. The I(D)/I(G) and I(2D)/I(G) ratios are calculated using the height of the D, 2D and G peak intensities. For each sample ~20 spectra are collected. The graphitic inks are diluted 1:10 with pure NMP and ethanol and drop-cast onto a Si wafer (LDB Technologies Ltd.) with 300 nm thermally grown SiO_2.

X-ray photoelectron spectroscopy (XPS) characterization is performed on a Kratos Axis Ultra DLD spectrometer, using a monochromatic Al Kα source (15 kV, 20 mA). Samples for XPS measurements are prepared by drop casting the two graphitic inks in NMP and ethanol onto silicon wafers. Wide scans are acquired at analyser pass energy of 160 eV. High-resolution narrow scans are performed at constant pass energy of 10 eV and steps of 0.1 eV. The photoelectrons are detected at a take-off angle (*i.e.*, the angle defined by the sample surface normal and the position of the detector) $\Phi = 0°$ with respect to the surface normal. The pressure in the analysis chamber is maintained below 9×10^{-12} bar for data acquisition. The data are converted to VAMAS format and processed using CasaXPS software, version 2.3.16. Fitting of the N 1s spectrum is performed using a linear background and Voigt profiles.

Electrodes fabrication

The Cu foil with thickness of 25 µm (Sigma-Aldrich) is cut into round shape disks with diameter of 1.5 cm and cleaned with acetone (Sigma-Aldrich) in ultrasonic bath for 10 min. Then, the Cu foils are dried at 80 ˚C and 10^{-3} bar for 2 hours in a glass oven (BÜCHI, B-585) and weighted afterward (Mettler Toledo XSE104). Subsequently, 250 µL of graphene ink in ethanol is drop-cast on Cu foil under air atmosphere at RT (see Fig. 1 (d)) and then dried at 120 ˚C and 10^{-3} bar for 30 min in oven (BÜCHI, B-585). The graphene mass loading (1 mg) for each anode is calculated by subtracting the weight of bare Cu foil from the total weight of the electrode.

Electrodes characterization

Scanning electron microscopy (SEM) analysis of the inks is carried out by means of a field-emission scanning electron microscope FE-SEM (Jeol JSM-7500 FA). As-prepared inks are drop cast with a pipette on the surface of silicon wafer and imaged without any metal coating.

The thickness of the graphitic film deposited on Cu is measured by means of a Dektak XT profilometer (Bruker) equipped with a diamond-tipped stylus (2 µm) selecting a vertical scan range of 15 µm with 8 nm resolution and a stylus force of 1 mN, on area of~0.25 cm^2.

Raman spectroscopy on the as prepared electrodes is carried out in the same experimental conditions reported for the characterization of the inks.

Specific surface-area measurements are carried out by nitrogen physisorption at 77 K in a Quantachrome equipment, model autosorb iQ. The graphene-based anodes deposited onto the Cu support substrates are cut into pieces fitting into the BET measurement chamber. The specific surface area is calculated using the multi-point BET (Brunauer–Emmett–Teller) model, considering 11 equally spaced points in the P/P_0 range from 0.05 to 0.30. Prior to measurements, the sample is degassed for 2 hours at 200 °C under vacuum to eliminate adsorbates.

Assembling of half- and full-cells

Both the half- and full-cells are assembled in coin cells (2032, MTI) in an argon-filled glove box (O_2 and $H_2O<0.1$ ppm) at 25 °C, using 1 M $LiPF_6$ in a mixed solvent of ethylene carbonate/ dimethylcarbonate (EC/DMC, 1:1 volume ratio) as electrolyte (LP30, BASF) and a glass fibre separator (Whatman GF/D). For the half-cell configuration, the anodes are tested against Li foil (Sigma-Aldrich) circular electrodes. The cathode used in the full cell is prepared using commercial LNMO powder (NEI Corporation). The cathode composition is: 80 wt% of LNMO, 15 wt% of carbon black (Super-P, TIMCAL) and 5 wt% PVdF (MTI). The three components, in form of powders, are mixed with NMP using a ball mill at 250 rpm for 2 hours. The obtained slurry is then deposited, by doctor-blade, on KOH-etched aluminium foils. To promote a better adhesion between the cathode slurry and the current collector, the roughness of Al foils was increased by an etching procedure in KOH. To this end, the Al foils were immersed for 1 minute in a 5 wt.% KOH aqueous solution, and afterward carefully washed with distilled water and dried at 60 °C for 4 hours. After the drying process, the electrodes are shaped in circular form by a cutting procedure, followed by a pressing process at ~2 MPa for 1min. Before full-cell assembling, the anode is pre-lithiated[30] by placing the graphitic film in direct contact with a Li foil wet by the electrolyte solution for 30 min.

Electrochemical characterization

The cyclic voltammetries (CVs) are performed at a scan rate of 50 μVs^{-1} between 1 V and 5 mV vs Li^+/Li with a Biologic, MPG2 potentiostat/galvanostat. All the electrochemical measurements are performed at RT. Constant current charge/discharge galvanostatic cycles are performed for the as prepared binder-free anodes in half-cell and in full-battery configurations at different conditions (see details in section "Electrochemical properties of the electrodes") using a battery analyser (MTI, BST8-WA).

Results and discussion

Inks and electrodes preparation

Inks are prepared by LPE of graphite in NMP,[36] having a surface tension (41.2 mN m^{-1})[70] close to the graphene surface energy (46.7 mN m^{-1}).[36, 37, 55] Graphite is exfoliated by ultrasonication process,[71,72] producing a heterogeneous dispersion of thin/thick and small/large graphitic flakes.[35] The resulting dispersion is subsequently ultracentrifuged exploiting the sedimentation-based separation (SBS) process,[30, 73] to obtain an ink enriched in single- (SLG) and few-layer (FLG) graphene flakes. The as obtained NMP ink could, in principle, already be deposited on the current collector to form a graphene-based anode for LIB.[30] However, the high boiling point of NMP (202 °C)[40] poses limitations especially in view of industrial production, which requires an effective and fast (within a few minutes) deposition process.[51-58] To overcome such issue, we have exploited a solvent exchange process[65] from NMP to a low boiling-point and more environmentally-friendly solvent such as ethanol. The exchange of graphene flakes from NMP into ethanol[74] promotes the precipitation of the graphene flakes due to its low surface tension (~22 mNm^{-1})[36] with respect to the surface energy of graphene,[36] and results in a metastable ink in ethanol. Fig. 2 plots the OAS of the graphitic-based NMP ink prepared via SBS. The UV absorption peak located at ~275 nm can be attributed to inter-band electronic transitions from the unoccupied π^* states at the M point of the Brillouin zone.[72, 75] Using the experimentally derived absorption coefficient of 1390 $Lg^{-1}m^{-1}$ at 660 nm,[30, 36] we estimate a concentration of graphitic flakes of ~0.18 g L^{-1}. For the estimation of the concentration of the graphitic flakes in the ethanol-based ink, we use a direct method: the average mass loading of the graphitic film (1 mg), after solvent evaporation, is divided by a known volume (250 µL) of the drop-cast ethanol-based ink onto the Cu foil. Following this procedure we estimate a concentration of graphitic flakes of ~5.6 g L^{-1} in the ethanol-based ink, which is ~30 times higher than the one achieved in NMP. The high concentration of the graphitic flakes in the ethanol-based ink enables the fabrication of anodes using a simple one-step process by directly drop-casting the as obtained graphitic flakes onto a Cu foil followed by drying at RT. Moreover, the solvent exchange process allows recycling over 90 % of NMP, decreasing production costs, waste disposal and pollution.

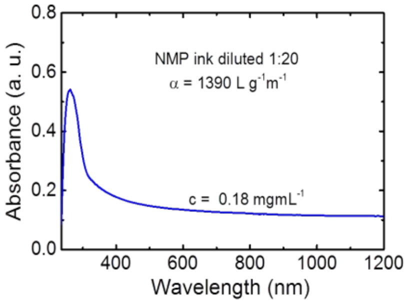

Figure 2. Absorption spectra of the graphene ink in NMP.

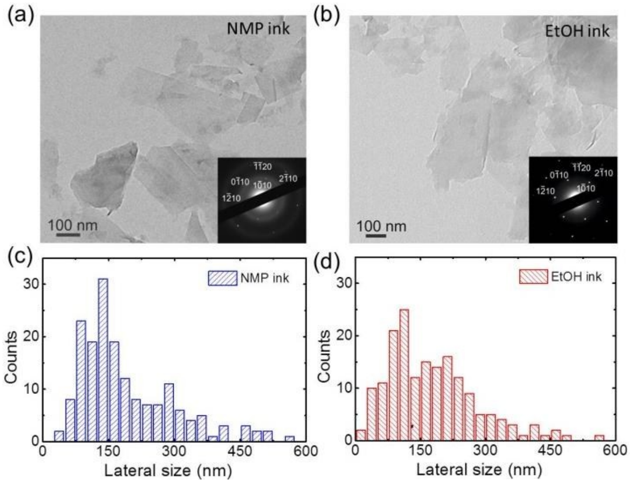

Figure 3. Bright-field TEM image of graphene flakes dispersed from the (a) NMP ink and (b) Ethanol ink; the insets show the electron diffraction patterns collected on an area of 2 µm in diameter with the peaks labelled by Miller–Bravais indices. (c) and (d) Lateral size distribution, extracted by statistical analysis on TEM images, of graphene flakes dispersed in NMP (blue) and after solvent exchange in ethanol (red).

The morphological properties of the graphitic flakes dispersed in the NMP-based ink and in the ethanol-based ink are characterized by means of TEM and Raman spectroscopy. Transmission electron microscopy bright field images of the graphitic flakes before (NMP) and after solvent exchange (ethanol) process are reported in Figs. 3(a) and (b), respectively. Both samples are formed by graphitic flakes with an average lateral size in the 100-150 nm range, (see

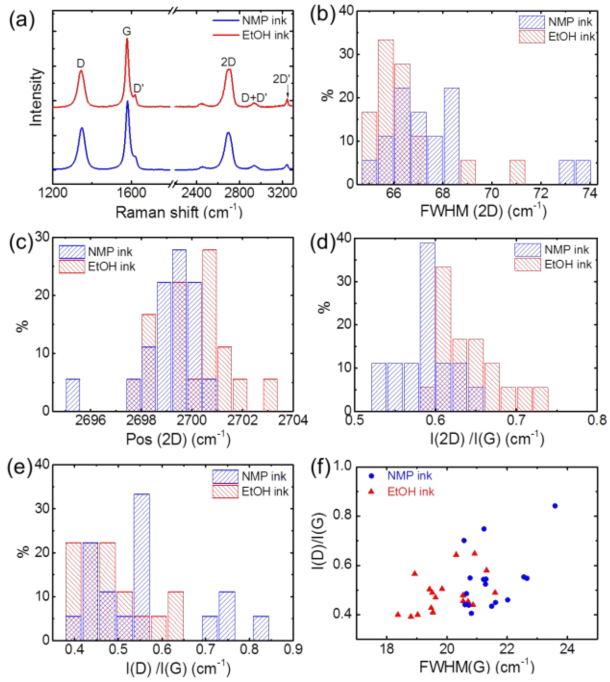

Figure 4. (a) Raman spectra at 532 nm excitation wavelength for representative flakes in NMP ink (blue curve) and ethanol ink (red curve). Distribution of (b) FWHM(2D), (c) Pos(2D), (d) I(2D)/I(G), (e) I(D)/I(G), and (f) distribution of I(D)/I(G) as a function of FWHM(G), for NMP ink (blue dashed histograms and dots) and ethanol ink (red dashed histograms and triangles), respectively.

Figs. 3(c) and 3(d) for statistical analysis). The statistical analysis demonstrates that the solvent exchange process does not induce modification in the lateral size of the graphitic flakes. Electron diffraction patterns, shown in the inset to Fig. 3(a) and 3(b), collected on flakes aggregates indicate that the flakes are crystalline in both samples. All the rings are indexed as h,k,-h-k,0 reflections of an hexagonal lattice with a=0.244(1) nm, in agreement with the graphene structure.[73]

To gain insight into the number of layers in the flakes and presence of defects,[76, 77] we have carried out a Raman analysis. Fig. 4(a) plots the typical Raman spectra of the graphitic flakes deposited on Si/SiO_2 for both the NMP-based ink (blue curve) and the ethanol-based ink (red curve). In a typical Raman spectrum of graphene, the G peak corresponds to the E_{2g} phonon at the Brillouin zone center;[77] the D peak is due to the breathing modes of the sp^2 rings and requires a defect for its activation by double resonance;[78-81] the 2D peak is the second order of the D peak.[78] In pristine graphene, the 2D peak has a single Lorentzian component, whereas it splits (upshifting also in position) in multi-layer graphene, reflecting the evolution of the band structure.[78,82,83] An estimation of the number of layers of the flakes comes from a statistical Raman analysis (based on 20 measurements for both NMP-based ink and ethanol-based ink), of the full width at half maximum of the 2D peak (FWHM(2D)), see Fig. 4(b), the average position of the 2D peak (Pos(2D)) (Fig. 4(c)) and the I(2D)/I(G) ratio (Fig. 4(d)). While we

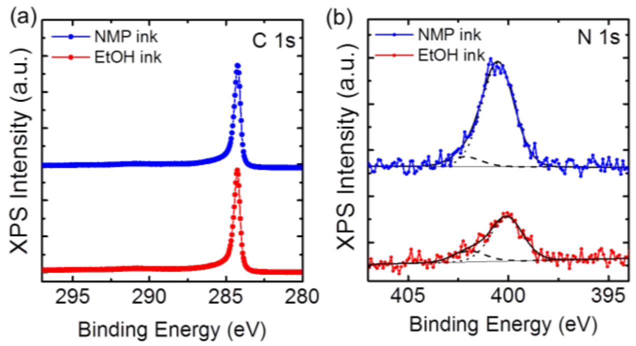

Figure 5. XPS data of the (a) C 1s and (b) N1s core-levels acquired on graphene films obtained from NMP and ethanol inks. N1s profiles are fitted as described in the experimental section and detailed in the text.

refer to Refs. 11, 30, 34 for more details about the procedure, we point out that a FWHM(2D) in average lower than 70cm^{-1}, Pos(2D) around 2700cm^{-1} and the ratio I(2D)/I(G) ratio higher than 0.5, the value for graphite,[78] indicate that both samples are composed of a combination of SLG and FLG flakes.[11, 30, 34, 36] Additionally, the Raman spectra show significant D peaks intensities (Fig. 4(e)). However, we attribute the high I(D)/I(G) ratio to the edges of our sub-micrometer flakes,[79] (see Fig. 3) rather than to the presence of a large amount of defects within the flakes, otherwise the D peak would be much broader, and G, D' would merge in a single band.[77] Indeed, FWHM(G) always increases with defects.[77] As detailed in refs 11, 30, 34, 36 the lack of a clear correlation between I(D)/I(G) and FWHM(G) in both samples (Fig. 4(e)), further supports the absence of structural defects also after the solvent exchange process.

In order to gain further information about the surface chemistry of the SLG/FLG-based films deposited before and after the solvent exchange process, we investigated the two inks by XPS. We focused our analysis on the C 1s and N 1s core-levels to obtain information on the chemical state and the atomic bonding of the two elements (Fig. 5). Indeed, the shape and position of C 1s peak can provide information on the local environment and oxidation states of graphene, since binding energies are sensitive to the chemical environment.[84] The C 1s profiles collected on the two samples are reported in Fig. 5(a): in both cases, C 1s has an asymmetric shape with the C-C component centred at ~284.3 eV, as typically reported for pristine (*i.e.*, unoxidized) graphene and graphite flakes.[85, 86] The peak shape and the absence of a C-O component, usually centred at ~286.2 eV, prove that the SLG and FLG flakes have not undergone oxidation during either the exfoliation or the solvent exchange process.[36, 87] Nitrogen is present in very low content in both samples, as shown in Fig. 5(b): the N:C atomic ratio is 0.8:100 for the NMP ink, while it decreases to 0.4:100 after the solvent exchange process. For both NMP- and ethanol-based inks, the N 1s signal can be fitted with two components (Fig. 5(b)). The main component (dotted Voigt profiles) is centred at (400.3 ± 0.3) eV for both samples and can be assigned to pyrrolic N (*i.e.*, N coordinated as in the pyrrole molecule),[80] consistent with the presence of NMP molecules,[82, 88] likely trapped between the SLG and FLG flakes.[36] The

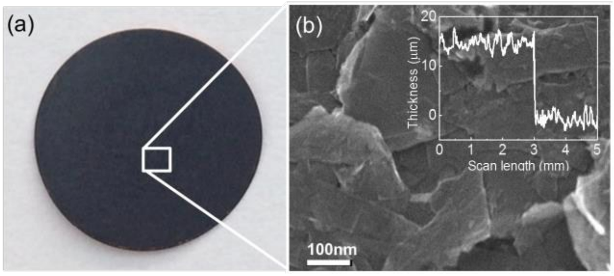

Figure 6. (a) Photograph of the Cu-supported SLG- and FLG-based electrode. (b) SEM image of graphene electrode. The inset shows the thickness of the SLG- and FLG-based electrode measured by a profilometer.

pyrrolic N component accounts for ~90 % and ~80 % of the total N content for the SLG and FLG flakes in the NMP-based inks and in the ethanol-based ink, respectively. The second, minor component (dashed profiles) is centred at 402.2 ± 0.3 eV, close to the position of the N peak observed in the related system of trimethylamine when adsorbed onto an electron acceptor substrate.[89] We therefore assign this component to the N of the NMP molecules adsorbed onto the SLG and FLG flakes.[90] In summary, the XPS analysis indicates that from one hand the solvent exchange process does not induce oxidation of the SLG and FLG flakes and from the other hand, it allows the removal of ~50 % of the NMP molecules adsorbed onto the SLG and FLG flakes, as determined *via* XPS analysis, see Fig. 5b. Such a small amount of residual NMP (less than 3.2 wt%, calculated from the N:C atomic ratio) demonstrates the feasibility of the proposed solvent exchange process for the NMP removal. The obtained results is remarkable considering that, in a previous work,[36] graphene flakes prepared in NMP ink have shown a residual content of NMP up to ~11 wt% even after a thermal annealing at 600 °C in high vacuum condition.

Anodes based on SLG and FLG flakes are then prepared by drop casting the ethanol-based ink onto Cu foil (see methods in Sect. 2.3 for experimental details). The as-produced electrodes have a mass loading of SLG and FLG flakes of 1 mg. The film covers homogeneously the Cu substrate, both at macroscopic (Fig. 6(a)) and microscopic (Fig. 6(b)) levels, with a thickness of ~15 µm (inset to Fig. 6(b)). The as-produced anode is also characterized by Raman spectroscopy in order to monitor the quality of the flakes composing the electrode. Fig. 7(a) compares a typical Raman spectrum measured at 532 nm for a flake deposited onto SiO_2 substrate from the ethanol-based ink, with that of the electrode. As for the inks (See Fig.4(f)) the absence of a correlation in the distributions of the I(D)/I(G) vs FWHM(G) (Fig. 7(b)) demonstrates that no additional defects on SLG and FLG flakes are caused by the deposition process.[88, 91, 92] Additionally, the 2D peak still shows a Lorentzian line-shape distinctly different from that of graphite. In fact, following Refs. 11, 30 the statistical analysis of I(2D)/I(G) (Fig. 7(c)) and Pos(2D) (Fig. 7(d)) of the as-prepared electrode indicates that the electrode is composed by a collection of SLGs and FLGs, which, also if stacked together, are however electronically decoupled.

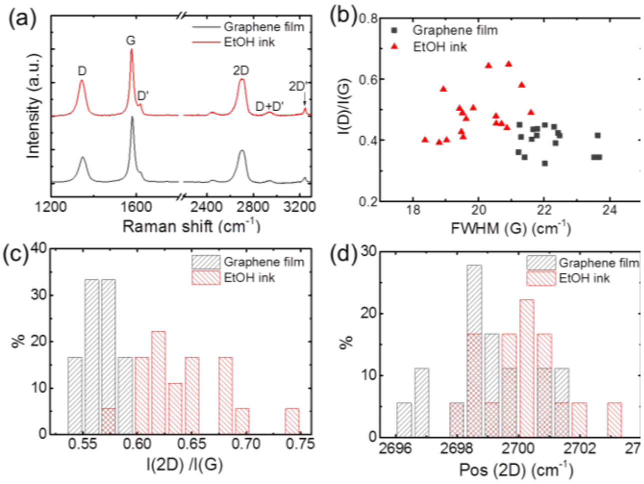

Figure 7. (a) Raman spectra of graphene ethanol ink (red) and the graphene electrode (dark gray), (b) I(D)/I(G) ratios as a function of FWHM(G), histograms of (c) I(2D)/I(G) and (d) Pos(2D).

Electrochemical properties of the electrodes

The anode electrodes based on SLG and FLG flakes are tested against metallic Li in a half-cell configuration, see method (sect. 2.5) for details. Figure 8(a) reports the cyclic voltammetries (CVs) performed at a scan rate of 50 µVs^{-1}, carried out to get a complete electrochemical response for Li ion transfer.[93] The scan range is from 1 V to 5 mV vs Li$^+$/Li, covering the formation of solid electrolyte interface (SEI)[94] and the lithiation/de-lithiation process for carbon material.[95]

The first CV scan shows a broad reduction peak with a maximum at ~0.55 V and an onset at ~0.8 V, which is associated to the SEI formation due to side reactions or the reduction of electrolyte at the surface of electrode.[94] The absence of this peak in the following scans indicates that the SEI formation is stable, guarantying a good cycle life of the anode, without further decomposition reactions.[94] Additionally, there is a current increase (~20 %) in the 0.1–0.3 V range passing from the 1st to the 5th cycle. This electrochemical behaviour can be associated to a slow activation of the lithiation/de-lithiation processes that gradually enhance the capacity of SLG/FLG flakes-based anode over cycling, as recently reported by Raccichini *et al.*[96] Our binder free electrode based on SLG and FLG flakes shows a specific capacity of 503 mAh g^{-1} at current density of 0.1 A g^{-1} after the 100th charge/discharge cycle in the range 50mV - 3V vs Li+/Li and a Coulombic efficiency of 99.5 % (Fig. 8(b)). Moreover, the device cycled at different current densities present excellent charge/discharge cyclability as well. In fact, a specific capacity of 610 mAh g^{-1} is reached when the graphene-based anode is cycled at 0.05 A g^{-1}. Additionally, specific capacity values of 260 mAh g^{-1} and 150 mAh g^{-1} have been reached after 20 cycles at current densities of 0.5 A g^{-1} and 1 A g^{-1}, respectively, see Fig. 8(b). Figure 8(c) presents the voltage profiles of the electrodes during the 1st, 10th, 50th and 100th galvanostatic charge/discharge cycles performed at current density of 0.1 A g^{-1} between 50 mV and 3 V vs Li$^+$/Li, in order to complete the

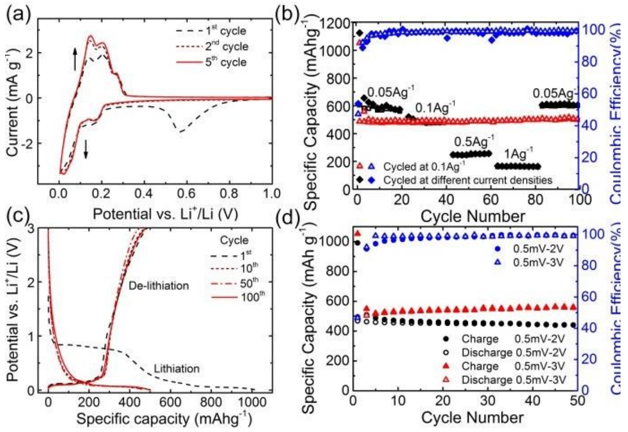

Figure 8. (a) Cyclic voltammetries at a scan rate of 50 µVs^{-1}. (b) Specific capacity and Coulombic efficiency over charge/discharge galvanostatic cycles between 50mV and 3V. The galvanostatic cycling at 0.1 A g^{-1} (triangles) is compared with the one at different current densities (diamond). (c) Voltage profile upon galvanostatic charge/discharge of graphene electrodes at 0.1 A g^{-1} between 50mV and 3V. (d) Specific capacity and Coulombic efficiency over galvanostatic cycles at current density of 0.1 A g^{-1} between 50mV and 2V (circle) and between 50mV and 3V (triangles), respectively.

lithiation/de-lithiation (charge/discharge) process in the SLG/FLG-based anode during each cycle. From the first voltage profile we can calculate an irreversible specific capacity of ~500 mAh g^{-1}, which represents about half of the total charge capacity. Such a high irreversible charge capacity value is typical for graphene-based anodes and it is presumably due to the large surface area[27, 28] (~325 m^2 g^{-1}, measured by BET) and edges reactivity of our SLG/FLG flakes with respect to graphite-based anodes.[97] The voltage profiles show that more than 50 % of the electrode capacity is delivered at a potential lower than 0.25 V vs Li$^+$/Li with a flat plateau up to the 100th cycle. Such a low potential is comparable to the values obtained using graphite (0–0.4 V vs Li$^+$/Li), leading to a high energy efficiency of batteries.[27] In order to understand the voltage cut-off on both the specific capacity and Coulombic efficiency of the graphene-based anode, we tested the electrode cycled at two different cut-off voltages, one between 50 mV and 2 V and the other one between 50 mV to 3 V. As shown in Figure 8(d), the specific capacities of the electrode tested in these two different voltage ranges are similar, with a capacity loss lower than 5% for the first 50 cycles for both test conditions. Also the Couloumbic efficiency is quite similar, with a value >99% achieved after 8 and 5 cycles for the electrode cycled up to 2 V and 3 V, respectively. Moreover, the electrode cycled up to 2 V shows no gradual increase of the specific capacity upon cycling as instead shown by the electrode cycled up to 3 V. As mentioned before, this specific capacity increase is linked to the slow activation of the anode.[96] It indicates that a small quantity of irreversible capacity, which may be related to the edges effects of the graphene flakes,[30] requires high voltage (2-3 V) to be completed.

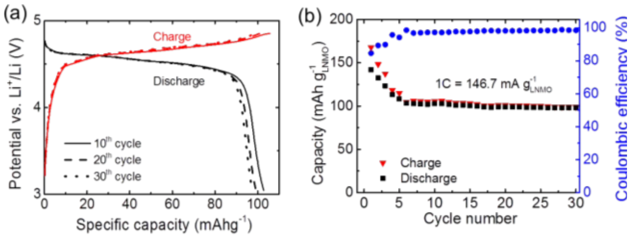

Figure 9. (a) Voltage profile upon galvanostatic charge/discharge of graphene/LNMO full battery. 10th, 20th and 30th cycle at 1 C (146 mA g^{-1} vs. LNMO). (b) Specific capacity and coulombic efficiency over charge/discharge galvanostatic cycles at 1 C between 3 V and 5 V of graphene/LNMO full battery.

Our binder-free SLG/FLG-based anode is further studied in LIB configuration, coupling it with a commercial cathode material, *i.e.*, LNMO. The latter is considered as one of the most promising candidates in the development of high energy/power LIBs,[98, 99] thanks to its high theoretical specific capacity (146.7 mAh g^{-1})[100] and high working voltage (around 4.7 V vs. Li$^+$/Li).[101] Before the full LIB assembly, we carried out a pre-lithiation step on the anode to improve the working voltage and the energy density as well as to reduce the irreversible capacity loss, increasing the Li$^+$ concentration of the electrolyte.[102] The aforementioned properties positively contribute to the cell cycling stability.[103] The reason behind the choice for the pre-lithiation process of the anode only for the full battery configuration and not for the half-cell configuration, relies on the fact that the LNMO cathode has limited Li$^+$ source compared to the metallic Li foil (used for the half-cell configuration tests).[102] Thus, the LNMO cathode is not able to provide sufficient Li$^+$ for the formation of SEI film without negatively affecting the cell cycling stability.[102] Moreover, in designing the battery, it is of paramount importance to reach an optimal balance of cathode and anode electrodes both in term of weight and electrochemical properties.[30, 102, 103] The weight ratio we used in trying to optimize the anode/cathode balancing is 1/3.5, which takes into account the difference in specific capacity of the two electrodes. As shown in Fig. 9(a), the SLGs/FLGs-LNMO full battery operates at a high voltage (~4.5 V) with a voltage profile similar to the typical LNMO one,[100] confirming appreciable anode performance with a substantially constant working voltage lower than 0.20 V vs. Li$^+$/Li.[101] The plot of the specific capacity as a function of the galvanostatic charge/discharge cycles (Fig. 9b) shows a rather stable specific capacity of ~100 mAh g^{-1} with respect to the mass of LNMO, and a Coulombic efficiency of ~99 % achieved after 5 cycles. A major drawback of the LNMO-based batteries is their capacity fade,[104, 105] which is caused by the decomposition of the electrolyte at the electrode/electrolyte interface at the high working voltage (~4.7 V).[104] The capacity and the stability of SLGs-FLGs/LNMO full battery are comparable to those of state of the art LNMO-based batteries.[76, 106-108] Although further research needs to be done on the optimization of LNMO cathodes and electrolyte, the results obtained by using the binder-free SLGs/FLGs-based electrodes, both in half- and full-cell configuration, strongly encourage their exploitation as advanced and high performance anode in LIBs.

Conclusions

In this work, a novel method for the fabrication of a binder-free SLGs/FLGs-based anode for LIBs is presented. The SLG and FLG flakes produced in NMP are then re-dispersed in ethanol by a solvent-exchange process. This approach leads to the several potential advantages in the production of anode electrodes for lithium batteries: (1) the presented SLGs/FLGs-based electrode is binder free. The use of~100 % in weight of active material in the anode provides remarkable electrochemical performance and stability; a charge/discharge specific capacity of 503 mAh g^{-1} after 100 cycles at a current density of 100 mA g^{-1} with a coulombic efficiency >99.5 %. Moreover, the SLG/FLG-based anode shows its functionality also in a full-cell configuration, exploiting commercial LNMO as cathode, with the working voltage around 4.7 V and a reversible specific capacity of~100 mAh g^{-1}; (2) the solvent exchange process appears as a fast, efficient and low-cost method to remove NMP from the SLG and FLG flakes forming the electrode; (3) the absence of any conductive agent and binder allows to use a simple, one-step process to deposit the SLGs/FLGs-based film, avoiding time-consuming and costly preparation procedures; (4) the exploitation of our solvent exchange process from NMP to ethanol reduces the pollution of dangerous chemicals during the electrode deposition, and it allows to recycle large part of the solvent (NMP) used during the graphite exfoliation process. When compared with other anodes used in LIBs technology, the one-step preparation route of SLGs/FLGs-based anode, herein proposed, opens the way to the improvement of both energy and power densities through a facile coating process, with consequent reduction of the environmental impact and production costs.

Acknowledgements

The authors acknowledge Massimo Colombo for BET measurements and funding from the European Union Seventh Framework Programme under grant agreement n°604391 Graphene Flagship.

Notes and references

1. F. Bonaccorso, L. Colombo, G. Yu, M. Stoller, V. Tozzini, A. C. Ferrari, R. S. Ruoff and V. Pellegrini, *Science*, 2015, **347**, 1246501.
2. J. B. Goodenough and K.-S. Park, *J. Amer. Chem. Soc.*, 2013, **135**, 1167-1176.
3. P. G. Bruce, B. Scrosati and J. M. Tarascon, *Angew. Chem. Int. Ed.*, 2008, **47**, 2930-2946.
4. M. Armand and J.-M. Tarascon, *Nature*, 2008, **451**, 652-657.
5. R. Schmalensee, T. M. Stoker and R. A. Judson, *Rev. Econ. Stat.*, 1998, **80**, 15-27.
6. B. Scrosati and J. Garche, *J. Power Sources*, 2010, **195**, 2419-2430.
7. P. G. Bruce, B. Scrosati and J. M. Tarascon, *Angew. Chem. Int. Ed.*, 2008, **47**, 2930-2946.
8. W. Van Schalkwijk and B. Scrosati, *Advances in lithium-ion batteries*, Springer Science & Business Media, 2002.
9. A. S. Arico, P. Bruce, B. Scrosati, J.-M. Tarascon and W. Van Schalkwijk, *Nature Mater.*, 2005, **4**, 366-377.
10. J. Liu and D. Xue, *Nanoscale Res. Lett.*, 2010, **5**, 1525-1534.
11. F. Torrisi, T. Hasan, W. Wu, Z. Sun, A. Lombardo, T. S. Kulmala, G.-W. Hsieh, S. Jung, F. Bonaccorso, P. J. Paul, D. Chu and A. C. Ferrari, *Acs Nano*, 2012, **6**, 2992-3006.
12. T. Marks, S. Trussler, A. Smith, D. Xiong and J. Dahn, *J. Electrochem. Soc.*, 2011, **158**, A51-A57.
13. M. Yoshio, R. J. Brodd and A. Kozawa, *Lithium-Ion Batteries*, Springer, 2009.
14. J. M. Tarascon and M. Armand, *Nature*, 2001, **414**, 359-367.
15. S. Flandrois and B. Simon, *Carbon*, 1999, **37**, 165-180.
16. C. Liu, F. Li, L. P. Ma and H. M. Cheng, *Adv. Mater.*, 2010, **22**, E28-E62.
17. E. Yoo, J. Kim, E. Hosono, H.-s. Zhou, T. Kudo and I. Honma, *Nano Lett.*, 2008, **8**, 2277-2282.
18. D. Wang, D. Choi, J. Li, Z. Yang, Z. Nie, R. Kou, D. Hu, C. Wang, L. V. Saraf and J. Zhang, *ACS Nano*, 2009, **3**, 907-914.
19. F. Cheng, J. Liang, Z. Tao and J. Chen, *Adv. Mater.*, 2011, **23**, 1695-1715.
20. C. K. Chan, H. Peng, G. Liu, K. McIlwrath, X. F. Zhang, R. A. Huggins and Y. Cui, *Nature Nanotech.*, 2008, **3**, 31-35.
21. L. Luo, P. Zhao, H. Yang, B. Liu, J.-G. Zhang, Y. Cui, G. Yu, S. Zhang and C.-M. Wang, *Nano Lett.*, 2015, **15**, 7016-7022.
22. C. K. Chan, X. F. Zhang and Y. Cui, *Nano Lett.*, 2008, **8**, 307-309.

23. P. Poizot, S. Laruelle, S. Grugeon, L. Dupont and J. Tarascon, *Nature*, 2000, **407**, 496-499.
24. D. Gu, W. Li, F. Wang, H. Bongard, B. Spliethoff, W. Schmidt, C. Weidenthaler, Y. Xia, D. Zhao and F. Schüth, *Angew. Chem. Int. Ed.*, 2015, **54**, 7060-7064.
25. Y. Li, B. Tan and Y. Wu, *Nano Lett.*, 2008, **8**, 265-270.
26. X. W. Lou, D. Deng, J. Y. Lee, J. Feng and L. A. Archer, *ADVANCED MATERIALS-DEERFIELD BEACH THEN WEINHEIM-*, 2008, **20**, 258.
27. R. Raccichini, A. Varzi, S. Passerini and B. Scrosati, *Nature Mater.*, 2015, **14**, 271-279.
28. M. Winter, J. O. Besenhard, M. E. Spahr and P. Novak, *Adv. Mater*, 1998, **10**, 725-763.
29. J. Cabana, L. Monconduit, D. Larcher and M. R. Palacin, *Adv. Mater.*, 2010, **22**, E170-E192.
30. J. Hassoun, F. Bonaccorso, M. Agostini, M. Angelucci, M. G. Betti, R. Cingolani, M. Gemmi, C. Mariani, S. Panero and V. Pellegrini, *Nano Lett.*, 2014, **14**, 4901-4906.
31. M. D. Stoller, S. Park, Y. Zhu, J. An and R. S. Ruoff, *Nano Lett.*, 2008, **8**, 3498-3502.
32. A. K. Geim and K. S. Novoselov, *Nature Mater.*, 2007, **6**, 183-191.
33. G. Fiori, F. Bonaccorso, G. Iannaccone, T. Palacios, D. Neumaier, A. Seabaugh, S. K. Banerjee and L. Colombo, *Nature Nanotech.*, 2014, **9**, 1063-1063.
34. A. C. Ferrari, F. Bonaccorso, V. Fal'ko, K. S. Novoselov, S. Roche, P. Boggild, S. Borini, F. H. L. Koppens, V. Palermo, N. Pugno, J. A. Garrido, R. Sordan, A. Bianco, L. Ballerini, M. Prato, E. Lidorikis, J. Kivioja, C. Marinelli, T. Ryhanen, A. Morpurgo, J. N. Coleman, V. Nicolosi, L. Colombo, A. Fert, M. Garcia-Hernandez, A. Bachtold, G. F. Schneider, F. Guinea, C. Dekker, M. Barbone, Z. Sun, C. Galiotis, A. N. Grigorenko, G. Konstantatos, A. Kis, M. Katsnelson, L. Vandersypen, A. Loiseau, V. Morandi, D. Neumaier, E. Treossi, V. Pellegrini, M. Polini, A. Tredicucci, G. M. Williams, B. Hee Hong, J.-H. Ahn, J. Min Kim, H. Zirath, B. J. van Wees, H. van der Zant, L. Occhipinti, A. Di Matteo, I. A. Kinloch, T. Seyller, E. Quesnel, X. Feng, K. Teo, N. Rupesinghe, P. Hakonen, S. R. T. Neil, Q. Tannock, T. Lofwander and J. Kinaret, *Nanoscale*, 2015, **7**, 4598-4810.
35. F. Bonaccorso, A. Lombardo, T. Hasan, Z. Sun, L. Colombo and A. C. Ferrari, *Mater. Today*, 2012, **15**, 564-589.
36. Y. Hernandez, V. Nicolosi, M. Lotya, F. M. Blighe, Z. Sun, S. De, I. McGovern, B. Holland, M. Byrne and Y. K. Gun'Ko, *Nature Nanotech.*, 2008, **3**, 563-568.
37. A. Capasso, A. E. D. R. Castillo, H. Sun, A. Ansaldo, V. Pellegrini and F. Bonaccorso, *Solid State Commun.*, 2015, **224**, 53-63.
38. P. Blake, P. D. Brimicombe, R. R. Nair, T. J. Booth, D. Jiang, F. Schedin, L. A. Ponomarenko, S. V. Morozov, H. F. Gleeson and E. W. Hill, *Nano Lett.*, 2008, **8**, 1704-1708.
39. S. Essig, C. Marquardt, A. Vijayaraghavan, M. Ganzhorn, S. Dehm, F. Hennrich, F. Ou, A. Green, C. Sciascia and F. Bonaccorso, *Nano Lett.*, 2010, **10**, 1589-1594.
40. PubChem, http://pubchem.ncbi.nlm.nih.gov/compound/1-methyl-2-pyrrolidinone#section=Top).
41. D. R. Lide, *CRC handbook of chemistry and physics*, CRC press, 2004.
42. M. Lotya, Y. Hernandez, P. J. King, R. J. Smith, V. Nicolosi, L. S. Karlsson, F. M. Blighe, S. De, Z. Wang and I. McGovern, *J. Amer. Chem. Soc.*, 2009, **131**, 3611-3620.
43. A. A. Green and M. C. Hersam, *Nano Lett.*, 2009, **9**, 4031-4036.
44. O. M. Maragó, F. Bonaccorso, R. Saija, G. Privitera, P. G. Gucciardi, M. A. Iatì, G. Calogero, P. H. Jones, F. Borghese and P. Denti, *ACS Nano*, 2010, **4**, 7515-7523.
45. A. O'Neill, U. Khan, P. N. Nirmalraj, J. Boland and J. N. Coleman, *J. Phys. Chem. C*, 2011, **115**, 5422-5428.

46. F. Bonaccorso, T. Hasan, P. Tan, C. Sciascia, G. Privitera, G. Di Marco, P. Gucciardi and A. Ferrari, *J. Phys. Chem. C*, 2010, **114**, 17267-17285.

47. K. G. Zhou, N. N. Mao, H. X. Wang, Y. Peng and H. L. Zhang, *Angew. Chem. Int. Ed.*, 2011, **50**, 10839-10842.

48. F. Bonaccorso and Z. Sun, *Opt. Mater. Express*, 2014, **4**, 63-78.

49. D. Zhou, Q.-Y. Cheng and B.-H. Han, *Carbon*, 2011, **49**, 3920-3927.

50. U. Halim, C. R. Zheng, Y. Chen, Z. Lin, S. Jiang, R. Cheng, Y. Huang and X. Duan, *Nature Commun.*, 2013, **4**.

51. D.-H. Ha, M. A. Islam and R. D. Robinson, *Nano Lett.*, 2012, **12**, 5122-5130.

52. W. Li, J. Zheng, T. Chen, T. Wang, X. Wang and X. Li, *Chem. Commun.*, 2014, **50**, 2052-2054.

53. H. X. Zhang, C. Feng, Y. C. Zhai, K. L. Jiang, Q. Q. Li and S. S. Fan, *Adv. Mater.*, 2009, **21**, 2299-2304.

54. B. Liu, X. Wang, H. Chen, Z. Wang, D. Chen, Y.-B. Cheng, C. Zhou and G. Shen, *Sci. Rep.*, 2013, **3**.

55. N. Li, S. Jin, Q. Liao and C. Wang, *ACS Appl. Mater. interfaces*, 2014, **6**, 20590-20596.

56. A. Abouimrane, O. C. Compton, K. Amine and S. T. Nguyen, *J. Phys. Chem. C*, 2010, **114**, 12800-12804.

57. S. Ng, J. Wang, Z. Guo, J. Chen, G. Wang and H. K. Liu, *Electrochim. Acta*, 2005, **51**, 23-28.

58. Y. Hu, X. Li, J. Wang, R. Li and X. Sun, *J. Power Sources*, 2013, **237**, 41-46.

59. I. Lahiri, S.-W. Oh, J. Y. Hwang, S. Cho, Y.-K. Sun, R. Banerjee and W. Choi, *ACS Nano*, 2010, **4**, 3440-3446.

60. B. Scrosati, J. Hassoun and Y.-K. Sun, *Ener. Environ. Sci.*, 2011, **4**, 3287-3295.

61. B. Dunn, H. Kamath and J.-M. Tarascon, *Science*, 2011, **334**, 928-935.

62. B. Scrosati, *Electrochim. Acta*, 2000, **45**, 2461-2466.

63. P. Bueno and E. Leite, *J. Phys. Chem. B*, 2003, **107**, 8868-8877.

64. S. Luo, K. Wang, J. Wang, K. Jiang, Q. Li and S. Fan, *Adv. Mater.*, 2012, **24**, 2294-2298.

65. I. Kovalenko, B. Zdyrko, A. Magasinski, B. Hertzberg, Z. Milicev, R. Burtovyy, I. Luzinov and G. Yushin, *Science*, 2011, **334**, 75-79.

66. E. Peled, D. Golodnitsky, G. Ardel and V. Eshkenazy, *Electrochim. Acta*, 1995, **40**, 2197-2204.

67. D. Aurbach, *J. Power Sources*, 2000, **89**, 206-218.

68. J. B. Goodenough and Y. Kim, *Chem. Mater.*, 2009, **22**, 587-603.

69. Y. T. Liang and M. C. Hersam, *J. Amer. Chem. Soc.*, 2010, **132**, 17661-17663.

70. M. Rosoff, *Nano-surface chemistry*, CRC Press, 2001.

71. M. T. J., *Oxford University*, 1999, **New York**, Chapter 1. .

72. D. Greenaway, G. Harbeke, F. Bassani and E. Tosatti, *Phys. Rev.*, 1969, **178**, 1340.

73. J. C. Meyer, A. K. Geim, M. Katsnelson, K. Novoselov, T. Booth and S. Roth, *Nature*, 2007, **446**, 60-63.

74. X. Zhang, A. C. Coleman, N. Katsonis, W. R. Browne, B. J. van Wees and B. L. Feringa, *Chem. Commun.*, 2010, **46**, 7539-7541.

75. V. Kravets, A. Grigorenko, R. Nair, P. Blake, S. Anissimova, K. Novoselov and A. Geim, *Phys. Rev. B*, 2010, **81**, 155413.

76. L. Yang, J. Deslippe, C.-H. Park, M. L. Cohen and S. G. Louie, *Phys. Rev. Lett.*, 2009, **103**, 186802.

77. A. C. Ferrari and D. M. Basko, *Nature Nanotech.*, 2013, **8**, 235-246.

78. A. Ferrari, J. Meyer, V. Scardaci, C. Casiraghi, M. Lazzeri, F. Mauri, S. Piscanec, D. Jiang, K. Novoselov and S. Roth, *Phys. Rev. Lett.*, 2006, **97**, 187401.

79. A. Ferrari and J. Robertson, *Phys. Rev. B*, 2001, **64**, 075414.

80. H. Nolan, B. Mendoza-Sanchez, N. A. Kumar, N. McEvoy, S. O'Brien, V. Nicolosi and G. S. Duesberg, *Phys. Chem. Chem. Phys.*, 2014, **16**, 2280-2284.

81. C. Thomsen and S. Reich, *Phys. Rev. Lett.*, 2000, **85**, 5214.

82. K. Neoh, E. Kang and K. Tan, *The Journal of Physical Chemistry B*, 1997, **101**, 726-731.

83. A. Das, S. Pisana, B. Chakraborty, S. Piscanec, S. Saha, U. Waghmare, K. Novoselov, H. Krishnamurthy, A. Geim and A. Ferrari, *Nature Nanotech.*, 2008, **3**, 210-215.

84. J. Matthew, *Surf. Interface Anal.*, 2004, **36**, 1647-1647.

85. B. Jiang, C. Tian, L. Wang, Y. Xu, R. Wang, Y. Qiao, Y. Ma and H. Fu, *Chem. Commun.*, 2010, **46**, 4920-4922.

86. A. V. Naumkin, A. Kraut-Vass, S. W. Gaarenstroom and C. J. Powell, NIST X-ray Photoelectron Spectroscopy Database http://srdata.nist.gov/xps/).

87. G. Eda, G. Fanchini and M. Chhowalla, *Nature Nanotech.*, 2008, **3**, 270-274.

88. H. Peng, F. Liu, X. Liu, S. Liao, C. You, X. Tian, H. Nan, F. Luo, H. Song and Z. Fu, *ACS Catal.*, 2014, **4**, 3797-3805.

89. X. Cao and R. J. Hamers, *J. Amer. Chem. Soc.*, 2001, **123**, 10988-10996.

90. J. Charlier, J. Cousty, Z. Xie, C. Poulennec and C. Bureau, *Surf. Interface Anal.*, 2000, **30**, 283-287.

91. T. Tsukamoto, K. Yamazaki, H. Komurasaki and T. Ogino, *J. Phys. Chem. C*, 2012, **116**, 4732-4737.

92. Y. Y. Wang, Z. H. Ni, T. Yu, Z. X. Shen, H. M. Wang, Y. H. Wu, W. Chen and A. T. Shen Wee, *J. Phys. Chem. C*, 2008, **112**, 10637-10640.

93. M. D. Levi and D. Aurbach, *J. Electroanal. Chem.*, 1997, **421**, 79-88.

94. P. Verma, P. Maire and P. Novák, *Electrochim. Acta*, 2010, **55**, 6332-6341.

95. N. A. Kaskhedikar and J. Maier, *Adv. Mater.*, 2009, **21**, 2664-2680.

96. R. Raccichini, A. Varzi, V. S. K. Chakravadhanula, C. Kübel, A. Balducci and S. Passerini, *J. Power Sources*, 2015, **281**, 318-325.

97. Á. Caballero and J. Morales, *Nanoscale*, 2012, **4**, 2083-2092.

98. D. Liu, W. Zhu, J. Trottier, C. Gagnon, F. Barray, A. Guerfi, A. Mauger, H. Groult, C. Julien and J. Goodenough, *RSC Adv.*, 2014, **4**, 154-167.

99. J. Hassoun, S. Panero, P. Reale and B. Scrosati, *Adv. Mater.*, 2009, **21**, 4807-4810.

100. J.-H. Kim, S.-T. Myung, C. Yoon, S. Kang and Y.-K. Sun, *Chem. Mater.*, 2004, **16**, 906-914.

101. Q. Zhong, A. Bonakdarpour, M. Zhang, Y. Gao and J. Dahn, *J. Electrochem. Soc.*, 1997, **144**, 205-213.

102. J. Zhang, Z. Shi and C. Wang, *Electrochim. Acta*, 2014, **125**, 22-28.

103. S. Sivakkumar and A. Pandolfo, *Electrochim. Acta*, 2012, **65**, 280-287.

104. S. Monaco, F. De Giorgio, L. Da Col, M. Riché, C. Arbizzani and M. Mastragostino, *J. Power Sources*, 2015, **278**, 733-740.

105. J. Song, D. W. Shin, Y. Lu, C. D. Amos, A. Manthiram and J. B. Goodenough, *Chem. Mater.*, 2012, **24**, 3101-3109.

106. L. Zhou, D. Zhao and X. D. Lou, *Angew. Chem. Int. Ed.*, 2012, **124**, 243-245.

107. J. C. Arrebola, A. Caballero, M. Cruz, L. Hernán, J. Morales and E. R. Castellón, *Adv. Funct. Mater.*, 2006, **16**, 1904-1912.

108. L. Yang, B. Ravdel and B. L. Lucht, *Electrochem. Solid-State Lett.*, 2010, **13**, A95-A97.

Binder-free graphene as advanced anode for lithium batteries

Haiyan Sun[a], Antonio Esau Del Rio Castillo[a], Simone Monaco[b], Andrea Capasso[a], Alberto Ansaldo[a], Mirko Prato[b], Duc Anh Dinh[a]; Vittorio Pellegrini[a], Bruno Scrosati[b], Liberato Manna[b] and Francesco Bonaccorso[a]*

Table of content

A binder-free graphene anode for Li-ion battery showing a reversible specific capacity of ~500 mAh g^{-1} after 100 cycles is demonstrated.